



HAL
open science

Building Practical Descriptors for Defect Engineering of Electrocatalytic Materials

Raphaël Chattot, Pierre Bordet, Isaac Martens, Jakub Drnec, Laetitia Dubau,
Frédéric Maillard

► **To cite this version:**

Raphaël Chattot, Pierre Bordet, Isaac Martens, Jakub Drnec, Laetitia Dubau, et al.. Building Practical Descriptors for Defect Engineering of Electrocatalytic Materials. *ACS Catalysis*, 2020, 10 (16), pp.9046-9056. 10.1021/acscatal.0c02144 . hal-02931378

HAL Id: hal-02931378

<https://hal.science/hal-02931378>

Submitted on 6 Sep 2020

HAL is a multi-disciplinary open access archive for the deposit and dissemination of scientific research documents, whether they are published or not. The documents may come from teaching and research institutions in France or abroad, or from public or private research centers.

L'archive ouverte pluridisciplinaire **HAL**, est destinée au dépôt et à la diffusion de documents scientifiques de niveau recherche, publiés ou non, émanant des établissements d'enseignement et de recherche français ou étrangers, des laboratoires publics ou privés.

Building Practical Descriptors for Defect Engineering of Electrocatalytic Materials

Raphaël Chattot, Pierre Bordet, Isaac Martens, Jakub Drnec, Laetitia Dubau, and Frédéric Maillard

ACS Catal., Just Accepted Manuscript • DOI: 10.1021/acscatal.0c02144 • Publication Date (Web): 13 Jul 2020

Downloaded from pubs.acs.org on July 14, 2020

Just Accepted

“Just Accepted” manuscripts have been peer-reviewed and accepted for publication. They are posted online prior to technical editing, formatting for publication and author proofing. The American Chemical Society provides “Just Accepted” as a service to the research community to expedite the dissemination of scientific material as soon as possible after acceptance. “Just Accepted” manuscripts appear in full in PDF format accompanied by an HTML abstract. “Just Accepted” manuscripts have been fully peer reviewed, but should not be considered the official version of record. They are citable by the Digital Object Identifier (DOI®). “Just Accepted” is an optional service offered to authors. Therefore, the “Just Accepted” Web site may not include all articles that will be published in the journal. After a manuscript is technically edited and formatted, it will be removed from the “Just Accepted” Web site and published as an ASAP article. Note that technical editing may introduce minor changes to the manuscript text and/or graphics which could affect content, and all legal disclaimers and ethical guidelines that apply to the journal pertain. ACS cannot be held responsible for errors or consequences arising from the use of information contained in these “Just Accepted” manuscripts.

1
2
3
4
5
6
7
8
9
10
11
12

Building Practical Descriptors for Defect Engineering of Electrocatalytic Materials

13 *Raphaël Chattot*^{†, ‡, *}, *Pierre Bordet*[⊥], *Isaac Martens*[‡], *Jakub Drnec*[‡], *Laetitia*

14
15
16 *Dubau*[†] and *Frédéric Maillard*^{†, *}
17
18
19
20
21
22
23
24

25 † Univ. Grenoble Alpes, Univ. Savoie Mont Blanc, CNRS, Grenoble INP, LEPMI,
26

27
28
29 38000 Grenoble, France
30
31

32
33 ‡ European Synchrotron Radiation Facility, ID 31 Beamline, BP 220, F-38043
34

35
36
37 Grenoble, France
38
39
40

41 ⊥ Univ. Grenoble Alpes, CNRS, Institut Néel, F-38000 Grenoble, France
42
43
44
45
46
47
48
49
50
51
52
53
54
55
56
57
58
59
60

1
2
3
4
5
6
7
8 KEYWORDS: Electrocatalysis; Oxygen Reduction Reaction; Defect Engineering;
9
10
11 Structural Disorder; Nanomaterials.
12
13
14
15
16
17
18
19
20
21
22
23
24
25
26
27
28
29
30
31
32
33
34
35
36
37
38
39
40
41
42
43
44
45
46
47
48
49
50
51
52
53
54
55
56
57
58
59
60

TEXT

Defect engineering has recently gained considerable interest in electrocatalysis by extending the portfolio of materials design strategies toward more efficient and sustainable nanocatalysts¹. This approach is highly versatile as the term 'defect' in crystallography refers to any interruption of the regular pattern defining a perfect crystal. As such, point defects (atomic vacancies, interstitial atoms, antisite defects) line defects (dislocations, disclinations), planar defects (grain boundaries, stacking faults, twinning, steps) or bulk defects (voids, pores, cracks) are a non-exhaustive list of structural parameters to be possibly tailored to meet a catalytic material functional specifications. In contrast to former approaches in electrocatalysis, within the defects engineering strategies, electrocatalytic properties are tuned locally not globally. Indeed, defects produce (simultaneous) local changes in key structural parameters relative to catalytic performance, such as site coordination, strain or chemical composition.

Historically, density functional theory (DFT) calculations, molecular dynamics and kinetic Monte Carlo simulations have been extensively used to connect the catalytic

1
2
3 site local environment to its catalytic properties from computational screening over the
4
5
6
7 trial-and-error approach ². These methods rely on the determination of catalytic site
8
9
10 electronic structure that can be further bridged to the catalytic performance through
11
12
13 the adsorption strength of reaction intermediates. Especially, for a given reaction
14
15
16
17 mechanism, focusing on the 'limiting' reaction step(s) in the frame of Sabatier principle
18
19
20 represents a remarkably powerful and efficient route toward the reduction of numerous
21
22
23
24 system variables to few 'key' reactivity descriptors ³. In case of the sluggish oxygen
25
26
27
28 reduction reaction (ORR) on Pt, which restricts the development of proton exchange
29
30
31 membrane fuel cells (PEMFC), the existence of so-called scaling relations between
32
33
34 the *O, *OH and *OOH intermediates adsorption strengths allows focusing on a single
35
36
37
38 of these adsorbate. In that frame, calculations predict the optimal ORR rate is obtained
39
40
41
42 by decreasing the adsorption energy of *O (or by extension *OH and *OOH) by ~0.2
43
44
45 eV (or ~0.1 eV) compared to Pt(111) ⁴. The pivotal correlation between adsorption
46
47
48 trends of reaction intermediates and catalytic sites electronic structure is described by
49
50
51
52 the *d*-band model introduced by Hammer and Nørskov ^{5,6}. Since from this principle,
53
54
55
56 the catalytic properties of a site can be determined completely by its electronic
57
58
59
60

structure, descriptors of the d -band ultimately become (electronic) reactivity descriptors.

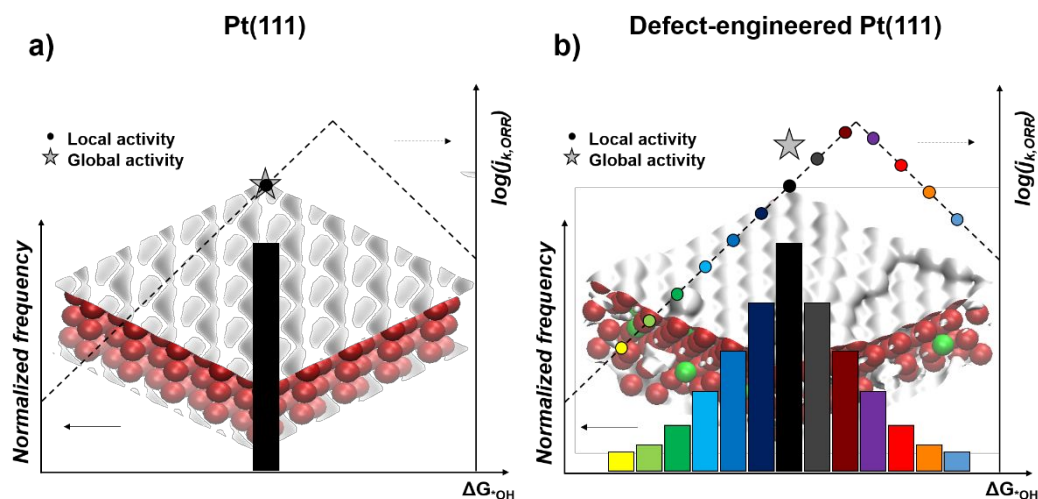


Figure 1. The defect engineering approach. Schematic representation principle of the narrow vs. near-continuous broad distributions of catalytic sites configurations and electrocatalytic performance for (a) ordered, model vs. (b) defective Pt(111) surfaces.

Fig. 1a illustrates how the d -band theory applies to a model Pt(111) surface, where all sites are equivalent (uniform coordination, interatomic distances and chemical environment). The surface thus features a Dirac type $*\text{OH}$ adsorption free energy ($\Delta G_{* \text{OH}}$) distribution, centered on the value expected for a single Pt(111) site, and its global activity (star symbol) can thus be virtually described by that of a single catalytic site (circle symbol). In contrast, Fig. 1b displays the situation when structural disorder is present at the surface (defect-engineered Pt(111) surface). Here, the coexistence

1
2
3 of sites with various local environments results in a broad, near-continuous distribution
4
5
6
7 of chemisorption properties ^{7,8}. Supposing the scaling relations still hold, this implies
8
9
10 that the global catalytic activity of the surface can no longer be described by that of a
11
12
13 single site, but rather as the average catalytic activity of each site. Consequently,
14
15
16
17 whereas the ORR activity of flat Pt(111) is limited by the overall too strong affinity with
18
19
20 *OH species (left branch of the volcano), a minority of catalytic sites with close-to-
21
22
23 optimal structural configuration, but exponential contribution to the global activity
24
25
26
27 (Butler-Volmer kinetics), ensures enhanced ORR activity for the defect-engineered
28
29
30 Pt(111) surface.
31
32

33
34
35 However, structure-sensitive, electronic descriptors alone (such as the d -band center,
36
37
38 ϵ_d) do not provide any clear-cut reverse structural information about the catalytic site
39
40
41
42 local environment that could guide material design. Also, even if computational
43
44
45 methods from model structures can correlate a fine local atomic motif and electronic
46
47
48 properties (see coordination-based descriptors such as \overline{CN} ⁹, CN^α ¹⁰ or \overline{CN}^{sd} ¹¹),
49
50
51
52 ensuring the successful implementation of such fine atomic motif onto practical
53
54
55 nanocatalysts surface remains extremely difficult. That is because (i) it requires an
56
57
58
59
60

1
2
3 atomic scale control of the surface structure design (other than atomically flat) and (ii)
4
5
6
7 characterization techniques are limited in describing such fine structural atomic motifs
8
9
10 on 'real-life' nanocatalysts. This apparent dichotomy between extremely fine
11
12
13 theoretical insights on well-defined systems and the extreme complexity of poorly
14
15
16 defined practical systems is at the heart of the defect engineering current challenge.
17
18
19
20 Whereas the uniformity of the catalytic sites was a convenient pillar of surface science,
21
22
23 here each surface atom has its own configuration and should be considered
24
25
26 individually (**Fig. 1**). In that frame, practical descriptors able to bridge surface
27
28
29 heterogeneous structure and catalytic performance experimentally are of primary
30
31
32 importance.
33
34
35
36
37
38

39 This viewpoint article intends to comment on the establishment of practical descriptors
40
41
42 able to guide the defect engineering of practical nanocatalysts. We first discuss the
43
44
45 case of the local strain, and especially how an explicit bulk physical parameter can be
46
47
48 turned to a surface structural descriptor: the surface distortion (SD). Then, we show
49
50
51 how cyclic voltammetry experiments analyzed in light of SD can reveal electrochemical
52
53
54 adsorption fingerprint of structural disorder, thus providing a versatile method to
55
56
57
58
59
60

1
2
3 shortcut in-depth structural characterization. Importantly, we emphasize that, because
4
5
6
7 structural or adsorption properties are averaged over the whole catalyst (*i.e.* the spatial
8
9
10 resolution is lost), such descriptors do not reveal the nature of the active site but mostly
11
12
13 provide statistical insights on their emergence from disorder. Consequently, we finally
14
15
16 discuss the opportunities offered by emerging analytical techniques we anticipate will
17
18
19 advance our understanding of defect characterization towards identification of
20
21
22 electrocatalytically active and stable motifs. Whereas Pt-based catalysts for PEM fuel
23
24
25 cell served as discovery platform of the presented methods, all results (except the
26
27
28 cyclic voltammetry techniques) apply to other types of nanocatalysts.
29
30
31
32
33
34
35
36
37
38
39
40
41
42
43
44
45
46
47
48
49
50
51
52
53
54
55
56
57
58
59
60

1
2
3
4 **1. Physical and electrochemical assessments of local strain to describe surface**
5
6
7 **disorder**
8
9

10 *Microstrain line broadening in powder X-ray diffraction*
11
12

13
14 Many phenomena synergistically contribute to the diffractograms profile observed in
15 powder X-ray diffraction (PXRD) experiments. As PXRD (especially from laboratory
16
17 sources) has become a routine technique in numerous fields of research, simple
18
19 analytical softwares have been developed to extract sample structural information
20
21 from PXRD data. However, extracting reliable information related to the quantification
22
23 of structural disorder requires a rigorous methodology to minimize the impact of errors
24
25 related to both experimental and interpretation artifacts. Numerous analytical
26
27 approaches such as Williamson-Hall method, Warren-Averbach method, Fourier
28
29 method or full profile refinement (Rietveld, Le Bail) methods can be used to investigate
30
31 the micro-structure of a powder sample from PXRD data. In case of nanocrystals with
32
33 sizes <10 nm, extensive peak broadening and overlap makes the methods based on
34
35 the analysis of few individual reflections inaccurate and full profile refinement
36
37 technique of PXRD patterns extending over a large Q -range are preferred (see Fig.
38
39
40
41
42
43
44
45
46
47
48
49
50
51
52
53
54
55
56
57
58
59
60

1
2
3
4 **2a).** This reason, together with the versatility offered by the full profile refinement
5
6
7 methods in terms of peak shape description and possible anisotropy consideration,
8
9
10 make the Rietveld method ¹² highly attractive, despite its complexity due to the large
11
12
13
14 number of control parameters.
15
16
17
18
19
20
21
22
23
24
25
26
27
28
29
30
31
32
33
34
35
36
37
38
39
40
41
42
43
44
45
46
47
48
49
50
51
52
53
54
55
56
57
58
59
60

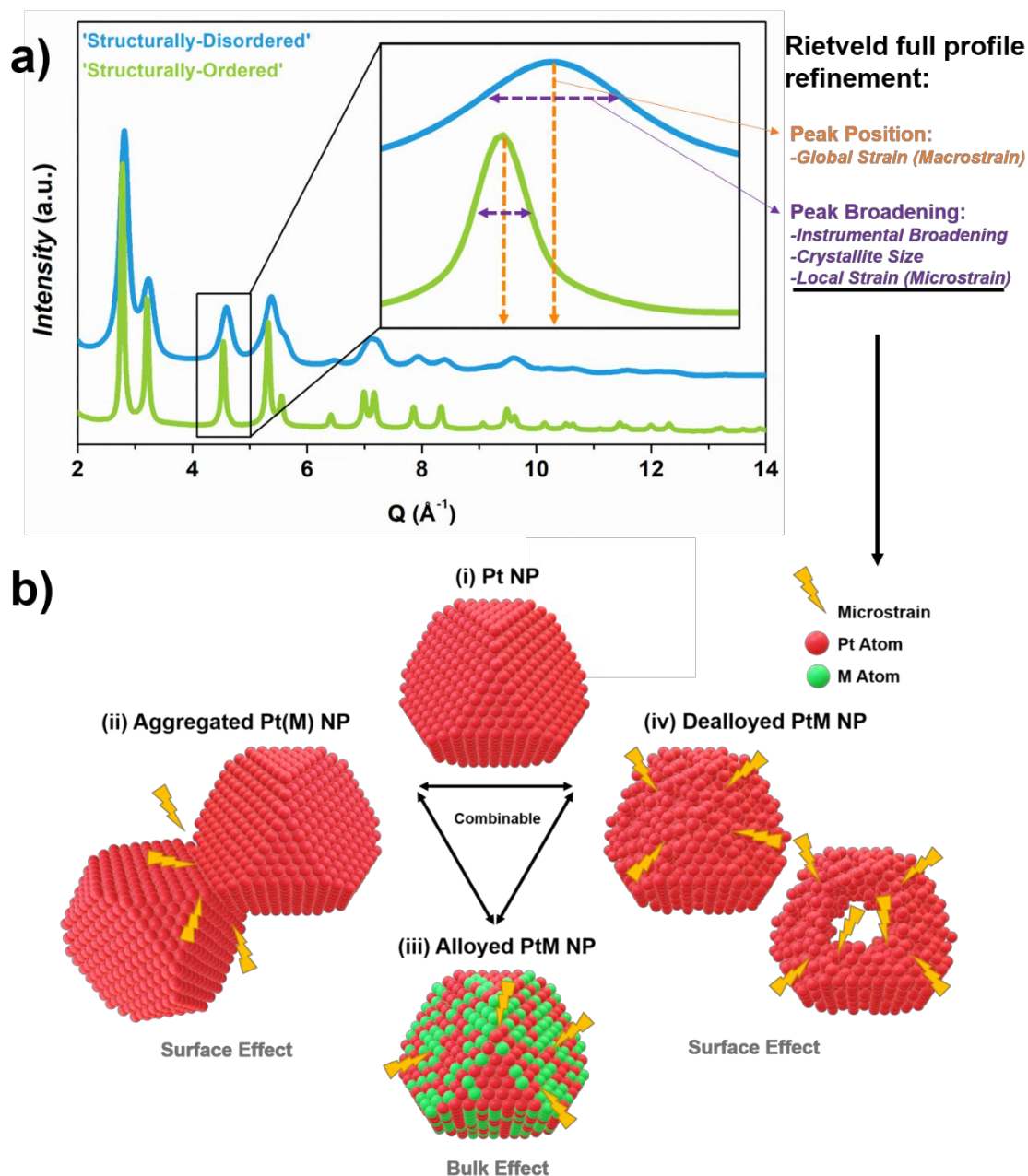


Figure 2. Powder X-ray diffraction (PXRD) patterns broadening and sources of microstrain in PtM nanoparticles (M being an early or late transition metal element). (a) Typical experimental PXRD patterns measured at the high energy ID31 beamline of the European Synchrotron Radiation facility on structurally disordered and structurally ordered catalysts (here hollow PtNi/C and cube Pt/C nanoparticles, respectively) plotted as a function of the momentum transfer Q . (b) Possible sources of microstrain in PtM nanocatalysts (grain boundaries, inhomogeneous alloying or (electro)chemical surface dealloying). The insert in (a) shows the influence of macrostrain, instrumental contribution and microstrain on the position and the broadening of the PXRD reflections. Adapted from Ref ¹³. Copyright 2018 Springer Nature.

1
2
3
4 It is generally admitted that the Bragg peak profile (shape and width) can be described
5
6
7 as the convolution of three contributions: (i) the incident X-ray beam monochromaticity,
8
9
10 (ii) the instrument optics (slit gaps and positions, detector pixel size *etc.*) and (iii)
11
12
13 sample-related broadening effects. The latter is the consequence of two
14
15
16 microstructural properties of the sample investigated, namely the finite size of the
17
18
19 coherent domains (or grain size), and the presence of microstrain (or local strain, the
20
21
22 parameter of interest here), which reflects the local variations of inter interplanar
23
24
25 distances caused by some sort of stress (disorder, stacking fault, twins, grain
26
27
28 boundaries, inhomogeneous alloying *etc.*, see **Fig. 2b**). As described in the Supporting
29
30
31 Information, the Rietveld method can disentangle microstrain broadening from other
32
33
34 contributions, thus providing a physical parameter that is representative of local strain
35
36
37 originating from structural disorder.
38
39
40
41
42
43
44
45

46 Rietveld refinement of powder X-ray diffractograms becomes limited when the
47
48
49 nanoparticle size is substantially smaller than the beam coherence length, (*i.e.*
50
51
52 typically a few nanometers ¹⁴) and a periodic crystal-type description of the atomic
53
54
55 arrangement breaks down, so as does the Bragg's law. In such case, Pair Distribution
56
57
58
59
60

1
2
3
4 Function (PDF) analysis of total scattering data can provide quantitative information
5
6
7 on the structural and microstructural properties of nanocatalysts ¹⁵. Experimentally,
8
9
10 the PDF is obtained from a PXRD pattern by realizing the Fourier transform as:

$$G(r) = 4\pi r [\rho(r) - \rho_0] = \frac{2}{\pi} \int_{Q_{min}}^{Q_{max}} Q [S(Q) - 1] \sin(Qr) dQ \quad (1)$$

11
12
13
14
15
16
17
18
19
20
21
22
23
24
25 Where $\rho(r)$ is the microscopic pair density and $Q = 4\pi \cdot \sin(\theta) / \lambda$. $S(Q)$ is the total
26
27
28 structure function, *i.e.* the normalized coherent scattered intensity obtained from the
29
30
31
32
33
34
35
36
37
38
39
40
41
42
43
44
45
46
47
48
49
50
51
52
53
54
55
56
57
58
59
60
PXRD pattern after subtraction of the environment and inelastic/incoherent scattering
and normalization. It is worth noting that the whole diffraction pattern is used to obtain
 $G(r)$, not only the Bragg peak intensities as for Rietveld refinement. Therefore, the
effects of disorder, defects, etc. which contribute to the pattern through diffuse
scattering outside of the Bragg peaks, will also be included in $G(r)$. The PDF yields the
probability of finding a pair of atoms separated by a distance r . It will oscillate in a way
that is characteristic of a given structure, about the average pair density that would
result from a completely unordered atomic arrangement. Thus, it can be calculated

1
2
3 from a structural model describing the distribution of atoms in a sample. The calculated
4
5
6
7 PDF can be fitted to the observed one, as in a 'direct space Rietveld refinement'. The
8
9
10 fit is carried out in a given interatomic distance range, yielding accurate structural
11
12
13 parameters relative to this range. Comparing refinements for very small or longer
14
15
16 distances allows revealing the presence of local structural distortions with respect to
17
18
19 an average long-range atomic arrangement. In addition, the PDF signal vanishes for
20
21
22 distances longer than the structural coherence length (or domain size), which provides
23
24
25 a simple way to determine the average nanoparticle size in a sample. On the other
26
27
28 hand, the effect of microstrain will be to broaden the distribution of interatomic
29
30
31 distances about their average values, which will result in a broadening of the
32
33
34 corresponding peaks of the PDF. The PDF is thus sensitive to microstrain, however
35
36
37 its effect is combined to thermal displacement and instrumental broadening, from
38
39
40 which it is difficult to extract. The PDF can also be used with Reverse Monte Carlo
41
42
43 minimization of large atomic assemblies, which allows a statistical description of
44
45
46 samples from liquids and amorphous to crystalline nanoparticles ¹⁶.
47
48
49
50
51
52
53
54
55

56 *From bulk microstrain to surface distortion*
57
58
59
60

1
2
3
4 The main reason to correct microstrain values is related to the definition of microstrain
5
6
7 itself, which links a local variation of the interplanar distance d between $d-\Delta d$ and $d+$
8

9
10 Δd according to:

$$\varepsilon = \frac{\Delta d}{d} \quad (2)$$

11
12
13
14
15
16
17
18
19
20
21
22
23
24
25 In practice, there is a distribution of $\Delta d/d$ within and across the coherent domains. The
26
27
28 refined ε value thus corresponds to the root mean square $\langle \varepsilon \rangle$, averaged over all
29
30
31 crystallites in the sample. Consequently, microstrain is a *global* and *relative* estimation
32
33
34 of structural disorder, since the even perfectly ordered domains ($\Delta d = 0$) also
35
36
37 contribute to the average value. To build a consistent structure-activity relationship in
38
39
40 heterogeneous catalysis, a *surface-specific* and *quantitative* structural descriptor is
41
42
43
44
45
46
47
48
49
50
51
52
53
54
55
56
57
58
59
60
60 measured microstrain values were proposed^{13,17}. These corrections derive from
experimental (electron microscopy observations^{18–23}) and theoretical studies^{8,13,24},

1
2
3 which suggest that microstrain can be decomposed into two main and independent
4
5
6
7 contributions:

- 8
9
10
11 - The surface microstrain mostly associated with the presence of grain
12
13 boundaries and/or arising from dealloying. Despite surface bound, such
14
15 microstrain values are relative and need to be corrected from the crystallite size;
16
17
18
19
20
21 - The microstrain of the whole crystallite volume (mostly arising from
22
23 heterogeneous alloying and hereafter referred as 'chemical disorder' in what
24
25 follows). Such microstrain is not representative of the surface and must be
26
27
28
29
30
31
32
33
34
35
36
37
38
39
40
41
42
43
44
45
46
47
48
49
50
51
52
53
54
55
56
57
58
59
60
- The surface microstrain mostly associated with the presence of grain boundaries and/or arising from dealloying. Despite surface bound, such microstrain values are relative and need to be corrected from the crystallite size;
 - The microstrain of the whole crystallite volume (mostly arising from heterogeneous alloying and hereafter referred as 'chemical disorder' in what follows). Such microstrain is not representative of the surface and must be estimated and subtracted.

As detailed in the Supporting Information, for PtM bimetallic catalysts, these hypotheses allow to decompose the measured microstrain as a sum of bulk chemical disorder ($f(\%M)$, estimated experimentally or from DFT calculations) and surface defectiveness (SD), weighted by the surface-to-volume ratio (D , calculated using Montejano-Carrizales *et al.*'s model ²⁵):

$$\text{Microstrain} = f(\%M) + D * SD \quad (3)$$

1
2
3
4
5
6
7
8 **Fig. 3** shows how the SD descriptor can be used to unveil the 'operating mode' of a
9
10 library of Pt and PtNi nanocatalysts. The ORR specific activity-SD plot in **Fig. 3.k**
11
12 indicates that enhanced ORR activity arises from two distinct approaches:
13
14
15
16
17
18

- 19 - The global surface tuning approach (null and low SD values), derived from DFT
20
21 calculations and single crystal studies, which aims at enhancing the ORR rate
22
23 by synthetically tailoring and maximizing the density of catalytic sites that
24
25 weakly chemisorb the ORR intermediates (in this category, octahedral PtNi
26
27 nanoparticles feature the highest ORR activity),
28
29
30
31
32
33
34
35
- 36 - The local surface tuning, or defect-engineering approach (high SD values), in
37
38 which the ORR rate is controlled by the fraction of catalytic sites with close-to-
39
40 optimal affinity to the ORR intermediates.
41
42
43
44
45
46
47
48
49
50
51
52
53
54
55
56
57
58
59
60

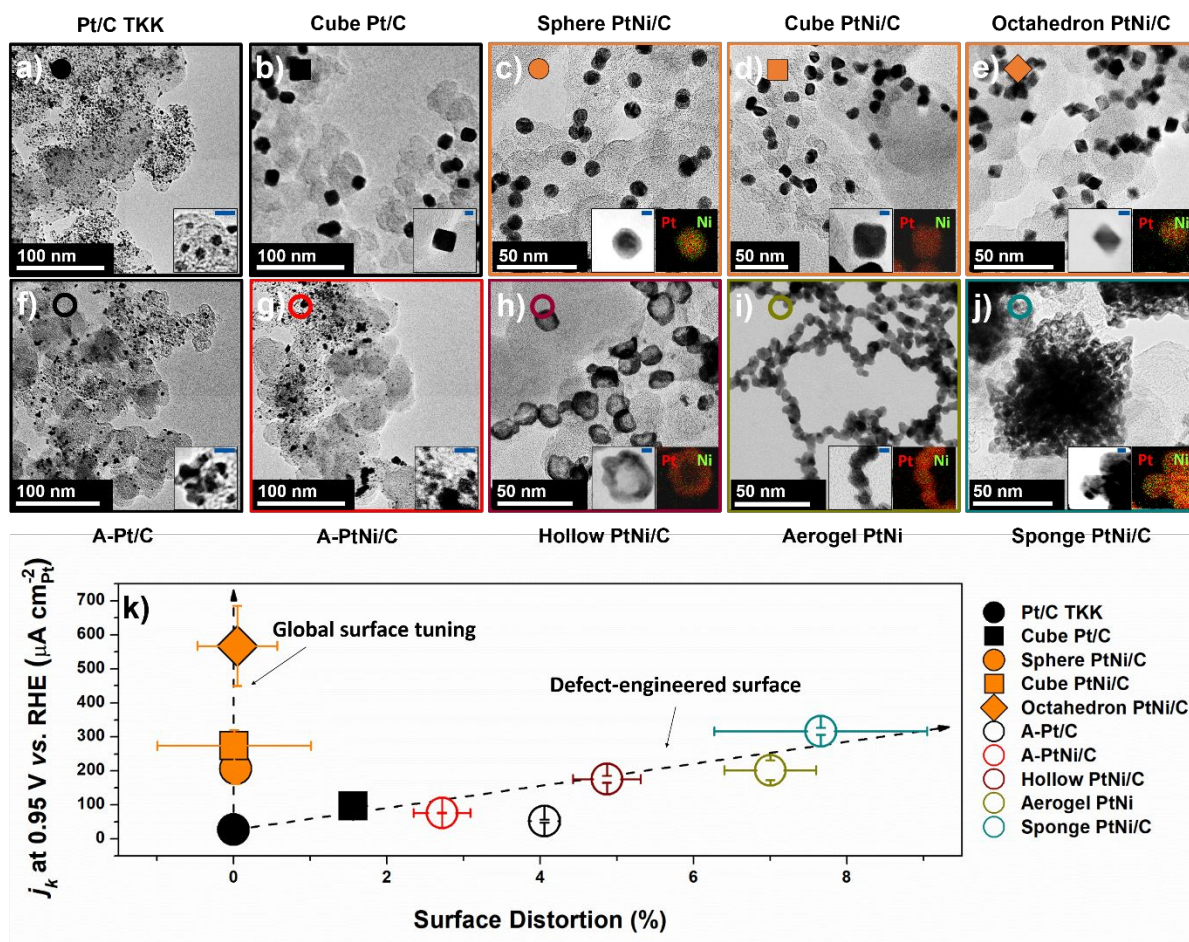


Figure 3. Using the SD descriptor to unveil the ‘operating mode’ of a variety of ORR nanocatalysts. (a-j) TEM images of the various nanostructures investigated. The inserts show higher magnification TEM or STEM/X-EDS elemental maps. (k) ORR activity measured at 0.95 V vs. RHE plotted as a function of the SD descriptor. The activity-SD plot quantitatively confirms that high ORR activity can be reached through the two approaches presented in Fig. 1. Panels (a-j) are reprinted with permission from Ref ²⁶. Copyright 2020 American Chemical Society. Panel (k) is adapted with permission from Ref ¹³. Copyright 2018 Springer Nature.

It is noteworthy that, as SD values are derived from microstrain values, they are only sensitive to the local strain caused by defects, and do not take into account other ORR-relevant fundamental parameters such as the average lattice contraction (global strain), the near surface chemical composition or the site coordination (that is why

1
2
3 multiple ORR activities can be found at low SD values). However, the fact that the
4
5
6
7 ORR activities increase almost linearly with the SD values (**Fig. 3.k**) is clear evidence
8
9
10 that, (i) similar to the 'classical' strain and ligand effects, surface disorder plays a key
11
12
13
14 role in ORR electrocatalysis and (ii) local strain alone is one, if not the most, influential
15
16
17 facets of disorder on catalytic performance.
18
19
20

21 Quantifying surface distortion from cyclic voltammetry

22
23
24
25
26 As discussed previously, the fundamental and direct consequence of structural
27
28
29 disorder is the emergence of a wide variety of catalytic site configurations on a given
30
31
32 electrocatalytic surface (**Fig. 1b**). DFT calculations by Le Bacq *et al.*^{8,13} have revealed
33
34
35 a ± 1 eV distribution width in *OH binding energy on structurally disordered Pt
36
37
38 surfaces. Whereas a fraction of these catalytic sites is statistically close to the optimal
39
40
41 configuration for a given catalytic reaction (~ 0.1 eV weaker chemisorption of *OH in
42
43
44 the case of the ORR), another fraction is in the optimal configuration for a different
45
46
47 reaction. Indeed, highly aggregated/polycrystalline nanocatalysts have demonstrated
48
49
50 desirable catalytic performances for a wide range of electrochemical reactions
51
52
53
54 including the ORR^{17,27-35}, the CO electrooxidation^{17,36}, the methanol or ethanol
55
56
57
58
59
60

1
2
3 electrooxidation ^{8,37-39}, the hydrogen evolution reaction (HER) and the OER ⁴⁰⁻⁴³.

4
5
6
7 Consequently, surface disorder and catalytic polyvalence must be somehow linked,
8
9
10 and similar SD-activity plot should be found for almost any reaction, at least involving
11
12
13
14 *OH species.

15
16
17
18 In that frame, CO_{ads} stripping (here referred to COOR) can be chosen as a
19
20
21
22 complementary reaction to the ORR to investigate surface catalytic polyvalence
23
24
25 because the prerequisite for optimal COOR are different regarding *OH adsorption
26
27
28 strength (increased *OH binding by ~0.4 eV relative to Pt(111) according to Calle-
29
30
31 Vallejo *et al.*) ⁴⁴. Simultaneous improvement in ORR and COOR specific activity should
32
33
34
35 consequently evidence catalytic polyvalence, and thus surface defectiveness. The
36
37
38
39 COOR activity (or CO tolerance) of a Pt-based nanocatalyst can be quantified by the
40
41
42 average CO_{ads} oxidation potential (μ_1^{CO} , or the first moment of the potential weight in
43
44
45 the CO_{ads} stripping voltammograms, see details in Ref ¹⁷ and examples in **Fig. 4a**).

46
47
48
49
50 As shown in **Fig. 4b**, a drawback of using complementary reactions to probe surface
51
52
53 catalytic polyvalence is that it is not generally applicable. If structural disorder must
54
55
56 induce catalytic polyvalence (μ_1^{CO} generally decreases with increasing SD), the inverse
57
58
59
60

1
2
3
4 is not necessarily true. Indeed, the COOR overpotential is not strictly governed only
5
6
7 by *OH adsorption strength, but by an appropriate balance between the formation of
8
9
10 *OH species and their combination with diffusing ⁴⁵ *CO species (Langmuir-
11
12
13 Hinshelwood mechanism). In practice, not only structural disorder but also crystallite
14
15
16 size, surface chemical composition and site coordination influence the *CO binding
17
18
19 energy, and thus the μ_1^{CO} values. A very good example of this was provided by
20
21
22 Stamenkovic *et al.* ⁴⁶, who reported simultaneous negative shift of the CO_{ads} stripping
23
24
25 profile and tremendous ORR activity for the Pt₃Ni(111)-skin surface, in agreement with
26
27
28 results from shape-controlled nanoparticles displayed in **Fig. 5b**, especially regarding
29
30
31
32
33
34
35 PtNi octahedra. A method relying only on *OH bond strength is consequently needed.
36
37
38
39
40
41
42
43
44
45
46
47
48
49
50
51
52
53
54
55
56
57
58
59
60

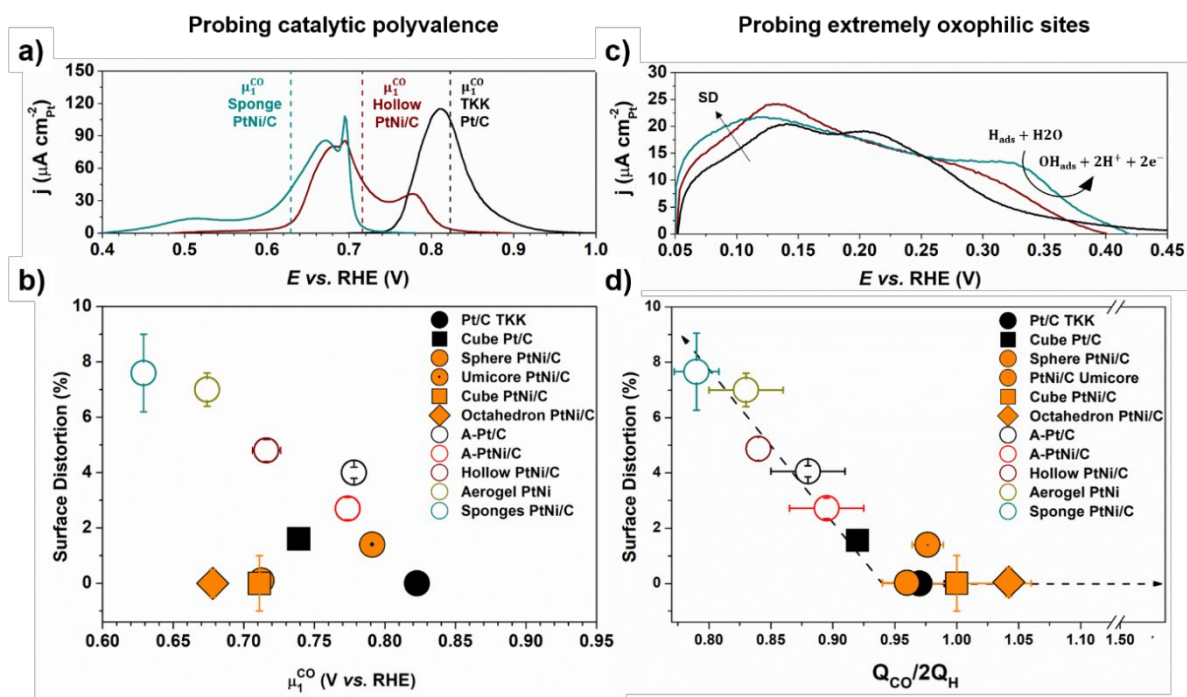


Figure 4. Probing catalytic sites diversity and oxophilicity. (a) Background-subtracted CO_{ads} stripping voltammograms recorded on Pt and PtNi nanomaterials featuring increasing SD values and their associated average potential μ_1^{CO} (dashed lines), (b) SD plotted as a function of the COOR activity (μ_1^{CO}) for a wide range of PtNi materials with different shape, size or Ni content. (c) background-subtracted H_{ads} desorption curves (so called- H_{UPD} region) of materials featuring increasing SD values pointing an extra electrochemical process at high potential ascribed to $^*\text{H}$ displacement by $^*\text{OH}$ on extremely oxophilic sites, and (d) SD plotted as a function of the ratio $Q_{\text{CO}}/2Q_{\text{H}}$ for a wide range of PtNi materials with different shape, size or Ni content. In (b), the numbers displayed close to the experimental points are the SD values associated to these catalysts. In both (a) and (c), the curves are normalized by the Pt surface area measured by CO_{ads} stripping. Panel (d) is adapted from permission of ref ²⁶. Copyright 2020 American Chemical Society.

It is deduced from the extremely low COOR onset potential observed in case of highly defective Sponge PtNi/C in Fig. 4a (~0.4 V vs. RHE) that $^*\text{OH}$ species are adsorbed on the surface at such low electrode potentials. The idea of concomitant adsorption of $^*\text{OH}$ and under-potentially deposited hydrogen (H_{UPD}) has been discussed many years

ago by Marichev *et al.* ⁴⁷, Van Der Niet *et al.* ⁴⁸, and more recently by Janik *et al.* ⁴⁹.

The results of infrared spectroscopy (IRAS) ⁵⁰ and CO displacement measurements ⁵¹ on extended surfaces, as well as DFT calculations, have suggested that *H species adsorbed on extremely oxophilic sites can be displaced by *OH species, following an electrochemical reaction of the type:



The displacement process described by **Eq. 4** creates an extra charge compared to the charge required just to desorb under-potentially deposited H atoms (Q_H). Consequently, an increase in Q_H compared to the CO_{ads} stripping charge (Q_{CO}), as experimentally observed in **Fig. 4c**, supports the presence of highly oxophilic sites on Pt-based surfaces ²⁶.

Most importantly, as displayed in **Fig. 4d**, contrary to μ_1^{CO} , the $Q_{CO}/2Q_H$ ratio measured on a wide range of nanocatalysts decreases almost linearly only with strictly positive values of SD, independently from other structural and chemical parameters. This suggests that such highly oxophilic sites are possibly generated only from structural disorder, *i.e.* there are not the 'simple' undercoordinated sites found at nanoparticles

1
2
3 surface edges, steps or kinks (otherwise, low $Q_{\text{CO}}/2Q_{\text{H}}$ ratio would be systematically
4
5
6
7 found on nanocatalysts). In other words, the $Q_{\text{CO}}/2Q_{\text{H}}$ ratio quantitatively probes the
8
9
10 fraction of highly oxophilic sites, which catalyze the process described by Eq. 4.

11
12
13
14 Because such extreme *OH adsorption energies are more likely reached *via* the
15
16
17 broadening of the *OH adsorption energies distribution than its simple uniform shift,
18
19
20 the ratio indirectly quantifies the structural disorder responsible for this broadening.
21
22

23
24 This hypothesis is supported by the SD- $Q_{\text{CO}}/2Q_{\text{H}}$ plot in Fig. 4d and the ORR activity-
25
26
27 $Q_{\text{CO}}/2Q_{\text{H}}$ plot in Fig. S2 of the Supporting Information, which show that, counter-
28
29
30 intuitively, the ORR activity increases with increasing fraction of highly oxophilic sites.
31
32

33
34
35 This result is of primary importance since the $Q_{\text{CO}}/2Q_{\text{H}}$ ratio can thus be used to
36
37
38 estimate the degree of surface defectiveness of a given catalyst, just as the
39
40
41 synchrotron X-ray based SD descriptor does, yet in a much more facile and accessible
42
43
44 way. Besides, this method is by definition truly surface sensitive, likely incorporating
45
46
47 the effects of coordination and/or chemical composition variations as well as local
48
49
50 strain. The method can also be employed *operando*, *i.e.* in a PEMFC device ²⁶.
51
52

53
54
55 Nevertheless, although these descriptors (SD and/or $Q_{\text{CO}}/2Q_{\text{H}}$) have a great
56
57
58 advantage to provide insights on the statistical existence of active atomic motifs over
59
60

1
2
3 the whole catalyst surface, the exact structure of these motifs and their location on the
4
5
6
7 surface remain largely unknown.
8
9

10 11 **2. Perspectives toward the identification of the active structural motifs** 12

13
14 In the previous section, we showed how the local strain averaged over the whole
15
16 catalyst surface could serve as a powerful structural descriptor to rationalize the
17
18 unique electrochemical behaviour of practical disordered surfaces. The SD descriptor,
19
20 in addition to the $Q_{CO}/2Q_H$ ratio, suggests that increasing surface disorder promotes
21
22 the emergence of only a fraction of active catalytic sites, in detriment of another
23
24 fraction. Further insights on the nature of these active sites (such as their location,
25
26 structural environment or which kind of defect generates them) would certainly guide
27
28 the optimization of defective nanocatalysts. In the following section, we review several
29
30 emerging analytical techniques that we believe will play a key role in that purpose.
31
32
33
34
35
36
37
38
39
40
41
42
43
44
45
46

47 *Electron microscopy tomography* 48

49
50
51 Recent advances in transmission electron microscopy (TEM) methodology regarding
52
53 spherical and chromatic aberration correction, improvements of cameras, electron
54
55 guns energy resolution and processing algorithms⁵² now allow the imaging and/or 3D
56
57
58
59
60

1
2
3 reconstruction of nanoparticles at the atomic scale. For example, using aberration
4
5
6
7 corrected scanning transmission electron microscopy (AC-STEM) operated in annular
8
9
10 dark field mode (STEM-ADF) tomography coupled with a generalized Fourier iterative
11
12
13 reconstruction (GENFIRE) algorithm, Yang *et al.*²² determined the coordinates of
14
15
16
17 each atom composing a face-centered tetragonal (L₁₀) PtFe nanoparticle (**Fig. 5a**).
18
19
20 Atomic coordinate determination represents the ultimate structural characterization
21
22
23 one can expect, and the results showed that a nominally ordered particle was in fact
24
25
26
27 composed of 8 individual grains, each featuring a different phase, including ordered
28
29
30 L₁₀ and L₂₀ or disordered face-centered cubic (*fcc*) phases. Each surface atom
31
32
33
34 coordination, local displacement compared to the perfect crystal structure and local
35
36
37
38 chemical environment can be determined from such measurements. Similarly, an
39
40
41 increasing number of studies^{18–23} have successfully mapped the distribution of strain
42
43
44
45 in extended surfaces or mono- and bi-metallic nanoparticles. Using high-resolution
46
47
48 scanning transmission electron microscopy (HRSTEM), Nilsson *et al.*²¹ have reported
49
50
51 that the bulk of Pt nanoparticles supported on alumina or ceria is (“rather”, as
52
53
54 employed by the authors) deformation-free. Interestingly, local strain was
55
56
57
58 systematically detected close to twin boundaries, at high surface curvature (convex
59
60

1
2
3 edge sites or concavities) and at the nanoparticle-support interface (see in **Fig. 5b**), in
4
5
6
7 agreement with other TEM studies ^{22,23,53,54}. In addition, the 'true' surface strain
8
9
10 distribution was directly deduced from the data, which constitutes an improvement
11
12
13 compared to SD that requires numerous hypotheses. This direct strain-defect type
14
15
16 correlation is precious for the defect engineering approach. It also evidences that
17
18
19 coordination and strain are strongly linked.
20
21
22

23
24
25 However, these measurements are extremely resource demanding and are usually
26
27
28 limited to a limited number of nanoparticles, which are supposed to be representative
29
30
31 of the whole catalyst. In addition, identical-location-aberration-corrected scanning
32
33
34 STEM (IL-AC-STEM) measurements ²³ evidenced that atomic coordinates measured
35
36
37 under TEM vacuum conditions change upon exposure to a PEMFC-relevant
38
39
40 electrochemical environment, which compromises the straightforward establishment
41
42
43 of valid structure-activity relationships from *ex situ* TEM imaging. Moreover, while
44
45
46 environmental *in situ* TEM methods are also progressing ⁵², the dramatic impact of
47
48
49 electron-irradiation on nanomaterials structure and chemistry in liquid cells is a major
50
51
52 issue that cannot be neglected ⁵⁵.
53
54
55
56
57
58
59
60

1
2
3
4 Atom probe tomography (APT)
5
6
7

8 Kelly *et al.*⁵⁶ have stated that « *The ideal microscope would reveal the position and*
9
10
11 *identity of all atoms in a specimen for as far as the user wishes to see*» and have
12
13
14 added that “*atom probes approach this ideal*”. APT is based on the evaporation of a
15
16
17 specimen atom by atom, layer by layer, from its surface by field effect; the ions being
18
19
20 further projected onto a position sensitive detector. The detector allows the
21
22
23 simultaneous determination of position and the element evaporated. The position and
24
25
26 the order of arrival of the ion impact on the detector allows one to reconstruct the
27
28
29 original position of the atoms on the initial tip and the time of flight of the ions contains
30
31
32 their elemental identity via the mass to charge ratio. The sample must be in the form
33
34
35 of a very sharp or a needle-shape tip. This is critical because the atoms are
36
37
38 progressively removed from the tip allowing the reconstruction of a 3D image of the
39
40
41 sample at the atomic scale. In relation with the concerns of the present paper, the
42
43
44 combination of highly sensitive composition measurement and three-dimensional
45
46
47 microstructural characterization represents a useful tool for the characterization of
48
49
50
51
52
53
54
55
56
57
58
59
60

1
2
3 structural defects. Indeed, APT has the unique capacity to study chemical segregation
4
5
6
7 to crystalline defects such as dislocations, stacking faults and grain boundaries ⁵⁷.
8
9

10
11 Recently, APT has met fundamental electrocatalysis. The oxidation/reduction
12
13
14 behavior of Pt-based alloys has been studied at different temperatures to show
15
16
17 preferential segregation effect of one metal. Oxidation of PtRhRu alloy was
18
19
20
21 dynamically been monitored, and it was shown that oxidation is initiated at grain
22
23
24 boundaries and propagates to form a Ru and Rh-rich oxide ⁵⁸. APT also revealed the
25
26
27 interplay between surface structure/composition, activity for oxygen evolution reaction
28
29
30
31 (OER) and stability of electrochemical Ir oxide ⁵⁹. At first stage of metallic Ir oxidation
32
33
34
35 by anodic polarization, the high OER activity was rationalized by the formation of non-
36
37
38 stoichiometric Ir oxide (IrO_x with $x < 2$) clusters composed of a very limited number of
39
40
41
42 atoms (only few tens) predominantly located at grain boundaries. This structure
43
44
45 gradually evolves towards more stable but less active IrO_2 . By combining isotope
46
47
48 labelling and APT, the same group has demonstrated that oxygen from the hydrated
49
50
51
52 Ir oxide participates in the formation of molecular oxygen, and that this mechanism
53
54
55 accelerates Ir dissolution ⁵⁹. Lastly, spatially resolved elemental compositions
56
57
58
59
60

1
2
3 achieved by APT have also demonstrated surface compositional changes of NiP
4
5
6
7 catalysts used to electrocatalyze the OER upon ageing in alkaline medium. The APT
8
9
10 results provided evidence of the complete depletion of P along with the presence of
11
12
13
14 amorphous and resistive NiO at the near-surface layers of the catalyst, and these
15
16
17 results were used to rationalize the OER activity decay ⁶⁰.

18
19
20
21 Nevertheless, APT sample preparation remains an issue to envision the use of this
22
23
24
25 technique in the (electro)catalysis field. The specific geometry of the APT tip (in the
26
27
28 form of a needle) with an end-tip radius of 30–100 nm is hardly compatible with powder
29
30
31
32 samples such as supported or even unsupported nanoparticles ⁶¹. Similarly, analysis
33
34
35 of porous materials usually designed by dealloying processes requires a specific
36
37
38 preparation. Pores and voids have to be previously filled to avoid overlapping ion
39
40
41 trajectories and distorted reconstructions induced by porosity ⁶². Nevertheless, these
42
43
44
45 recent results show that APT is a growing analytical tool in (electro)catalysis and its
46
47
48 emergence provides hope for detailed characterization of the topmost atomic surface
49
50
51 layers of nanostructured electrocatalysts, keeping in mind that APT overcomes the
52
53
54 main limitations of regular TEM. For example, Tedsree *et al.* ⁶³ successfully used APT
55
56
57
58
59
60

1
2
3
4 to reveal the internal structure of an Ag@Pd core@shell nanoparticle (Fig. 5c), where
5
6
7 the close proximity of Ag and Pd elements in the periodic table makes the imaging
8
9
10 contrast extremely challenging in TEM.
11

12 13 14 Advanced (coherent) X-ray methods

15
16
17
18
19 Beyond the averaged microstrain values extracted from PXRD, Bragg coherent
20
21
22 diffraction imaging (BCDI) is an emerging technique designed specifically for resolving
23
24
25 the 3D strain field inside individual nanocrystals using nanofocused X-rays⁶⁴ (see Fig.
26
27
28 **5d**). Strain fields inside a nanocrystal create phase shifts in the diffracted beam,
29
30 producing an interference pattern at the detector. A single 3D rocking curve coherent
31
32
33 diffraction pattern can recover 3D images of the electron density and strain inside Pt
34
35
36 nanoparticles. Complete datasets can be acquired on the order of minutes per
37
38
39 nanocrystal⁶⁵. Strain maps of single nanocrystals allow the structural influence of
40
41
42 individual crystal defects to be resolved. The strain field present at the surface of the
43
44
45 particle can be quantitatively determined, and different types of strain-inducing defect
46
47
48 structures can be visualized (*e.g.* vacancies from alloy leaching vs dislocation loops)
49
50
51
52
53
54
55

56
57
58 ⁶⁶.
59
60

1
2
3
4 The strain and real space resolutions of BCDI have benefited from ongoing
5
6
7 improvements in synchrotron brightness and coherent flux, and now approach those
8
9
10 of electron microscopy. The most significant advantage of X-ray based techniques is
11
12
13 that they can be performed *in situ*^{67,68} with much less beam damage artefacts, and
14
15
16 easier electrochemical control compared with TEM methods. The extremely small size
17
18
19 of commercial fuel cell Pt catalyst particles (<5 nm) remains, however, below the
20
21
22 present spatial resolution limit of BCDI, but shape-controlled model systems and other
23
24
25 electrocatalysts are already within reach⁶⁹. The phase sensitivity and strain resolution
26
27
28 in BCDI vastly exceeds the real-space electron density resolution of the nanocrystal.
29
30
31
32 More specifically, the presence of point defects can be detected, even when they
33
34
35 cannot be atomically resolved, because the locally induced strain field propagates
36
37
38 several unit cells away. The increased coherence of X-ray (nano)beams at 4th
39
40
41 generation synchrotron sources, such as the Extremely Brilliant Source (EBS) at the
42
43
44 European Synchrotron Radiation Facility (ESRF) are expectedly to rapidly advance
45
46
47 the ease and applicability of BCDI for *in situ* electrocatalyst strain imaging at the single
48
49
50 particle level, under the environment of a PEMFC device.
51
52
53
54
55
56
57
58
59
60

1
2
3
4 Complementarily, if one of the major advantages of high energy X-ray based
5
6
7 techniques over other methods is their ability to probe practical catalysts *in situ* or even
8
9
10 *operando*, the coherent diffraction imaging principles can be also applied to 'revisit'
11
12
13 model surfaces. The advantage over experiments on practical nanoparticle systems
14
15
16 is that specific defects can be introduced on single crystal surfaces in a well-controlled
17
18
19 manner, using techniques such as ion irradiation⁷⁰, cathodic atomization⁷¹, and
20
21
22 plasma or laser etching⁷². The structure of such model defect engineered surfaces
23
24
25 can be resolved *in situ* from surface X-ray diffraction⁷³ and electrochemical scanning
26
27
28 tunneling microscopy (EC-STM)^{74,75}. Coherent X-ray diffraction can also be used to
29
30
31 reconstruct the local strain fields on extended surfaces. Although experimental
32
33
34 protocols and X-ray methodology still require further development, the first steps in
35
36
37 this direction have already been taken^{76,77}.
38
39
40
41
42
43
44
45

46 One of the ultimate goals of nanofocused X-ray beam techniques is to study
47
48
49 nanostructured materials *in situ* and *operando* conditions utilizing the X-ray equivalent
50
51
52 of a TEM. The main advantage of direct, real space nanofocused beams over
53
54
55 reciprocal space imaging techniques is the ease of use and significantly simpler data
56
57
58
59
60

1
2
3
4 analysis, due to the lack of the diffraction phase problem. Currently, dedicated Dark-
5
6
7 field hard X-ray microscopy (DFXRM) instruments are being developed at ESRF ⁷⁸.
8
9

10 The first imaging results are encouraging, but the instrument still lacks the necessary
11
12
13
14 resolution to study catalyst particles in nanometre range. The spatial resolution
15
16
17 ultimately depends on the quality of the imaging lens, which is the current bottleneck.
18
19
20
21 However, recent developments in multilayer Laue lenses give hope that this obstacle
22
23
24 will be soon surpassed and imaging at the few-nanometre scale can be achieved in
25
26
27
28 the near future ⁷⁹.
29
30
31

32 *Electrochemical scanning tunneling microscopy noise measurements*

33
34
35

36 Whereas the various methods described above shed light on the complex local
37
38
39 structure of disordered surfaces, identification of the electrocatalytically active
40
41
42 sites/motifs is pivotal to the further development of the defect-engineering approach.
43
44
45
46 In that frame, it is worth pointing electrochemical scanning tunneling microscopy noise
47
48
49 measurements (n-ECSTM) first introduced by Pfisterer *et al.* in 2017 ⁸⁰. This technique
50
51
52
53 is based on the energy barrier difference for electrons tunneling from a sample to a
54
55
56
57 STM tip in aqueous electrolyte. The tunneling barrier is sensitive to all the molecules
58
59
60

1
2
3
4 present along the electrons' path, such as those adsorbed on the electrocatalytic
5
6
7 surface ⁸¹ and those diffusing to/from the electrochemical double layer ^{82,83}. Local
8
9
10 modifications of the tunneling barrier in turn allow identification of the most active sites
11
12
13 for a given reaction (**Fig. 5e**). The n-ECSTM technique revealed that Pt(111) terraces
14
15
16 best electrocatalyze the ORR in alkaline media ⁸⁴ and that step sites and concave
17
18
19 sites are the most active in acidic media ^{80,84}. Besides ORR, this technique revealed
20
21
22 that the edges of single MoS₂ and MoSe₂ flakes are more active than basal planes for
23
24
25 the hydrogen evolution reaction, but that the latter can be activated upon bombarding
26
27
28 with He-ions ⁸⁵.
29
30
31
32
33
34
35
36
37
38
39
40
41
42
43
44
45
46
47
48
49
50
51
52
53
54
55
56
57
58
59
60

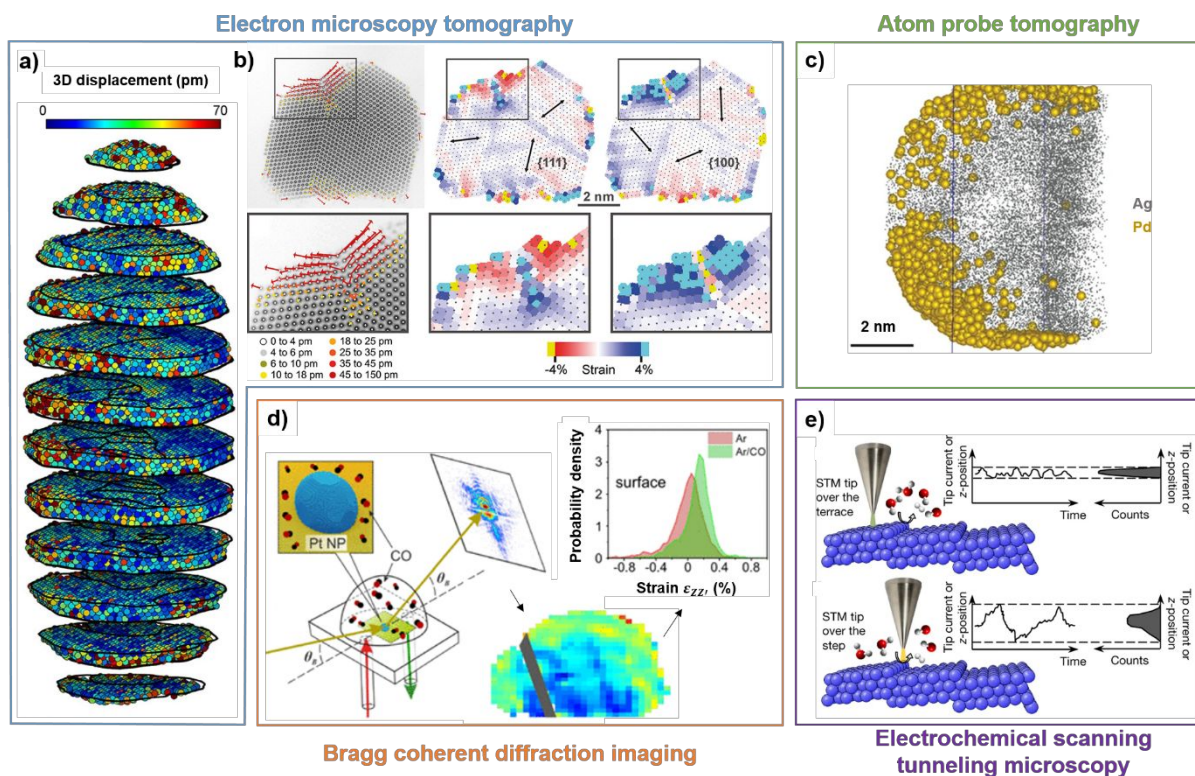


Figure 5. Determining the nature and structure of the catalytically active sites. (a) 3D atomic displacements measured in a FePt nanoparticle using GENFIRE algorithm from AC-STEM images; (b) Atomic resolution STEM images, with atomic displacement and strain maps within two crystallographic planes, as indicated in the Pt nanoparticle; (c) APT data showing the atom map from a Ag@Pd nanoparticle; (d) Sketch of the BCDI setup, 2D slice of the strain field through the center of a reconstructed Pt nanoparticle under Ar/CO flow and associated probability density of the strain field; (e) Scheme explaining the concept of using EC-STM noise analysis to reveal the catalytic sites under reaction conditions. Panel (a) is adapted with permission from Ref ²². Copyright 2017 Springer Nature. Panel (b) is adapted with permission from Ref ²¹. Copyright 2018 Springer Nature. Panel (c) is adapted with permission from Ref ⁶³. Copyright 2011 Springer Nature. Panel (d) is adapted with permission from Ref ⁶⁸. Copyright 2019 American Chemical Society. Panel (e) is adapted with permission from Ref ⁸⁰. Copyright 2017 Springer Nature.

CONCLUSION

In summary, the defect engineering approach has the particularity to touch the extreme complexity of nanoscale intrinsic structural disorder. Contrary to the ‘classical’

1
2
3
4 surface science approach, the connection between theoretical computations (and their
5
6
7 necessary simplifying assumptions) and experimental measurements on practical
8
9
10 systems is not yet established. Numerous theoretical descriptors have nonetheless
11
12
13
14 been applied to complex surfaces. For example, the generalized coordination number
15
16
17 (\overline{CN}) theory predicts the benefits of locally concave surface curvature, but without
18
19
20 considering the local strain possibly generated by surface roughness. On the contrary,
21
22
23
24 experimental observations (electron microscopy, X-ray diffraction) reveal significant
25
26
27
28 local strain in the vicinity of structural defects. From this factual result, local strain alone
29
30
31 (without considering the coordination effect) is a desirable experimental structural
32
33
34
35 descriptor of surface defectiveness, able to rationalize the electrochemical adsorption
36
37
38 behavior of disordered nanocatalysts, whereas each surface \overline{CN} remains hardly
39
40
41
42 accessible in practice.

43
44
45
46 Consequently, there are currently no clear theoretical guidelines driving the 'defective-
47
48
49 by-design' engineering of catalytic materials, and computational models must be
50
51
52
53 adapted to better describe experimental observations (and not the other way around).

54
55
56 Practical descriptors, however, suggest that maximizing surface distortion is an
57
58
59
60

1
2
3 efficient approach to boost catalytic performance, and the introduction of grain
4
5
6 boundaries or surface dealloying were identified as experimental levers to implement
7
8
9
10 such distortion. If practical structural descriptors inherit the limitations of their
11
12
13 characterization technique(s) (resolution, artefacts, (un)realistic sample environment
14
15
16 etc.), the constant technical development and fast progresses of instrumental tools
17
18
19
20
21 predict an ongoing improvement of their descriptive power.
22
23
24

25 Finally, one could reasonably think that the ultimate goal in the defect engineering
26
27
28 approach is to identify the structure of the most catalytically active site, and to
29
30
31 maximize its implementation on nanocatalyst surface. This would be missing an
32
33
34 important subtlety of this approach: the most active site is not necessarily desirable. It
35
36
37 depends on the compromise between the resulting site activity and the number of
38
39
40 (neighboring) sites that are 'sacrificed' to this purpose. This adds an extra layer of
41
42
43 complexity above the previously mentioned. One thing certain, there is still a lot to
44
45
46
47
48
49 uncover.
50
51
52
53
54
55
56
57
58
59
60

1
2
3
4 AUTHOR INFORMATION
5
6

7 **Corresponding Authors**
8
9

10 * E-mail for R.C.: raphael.chattot@grenoble-inp.org.
11
12

13
14 * E-mail for F.M.: frederic.maillard@lepmi.grenoble-inp.fr.
15
16
17
18
19
20
21
22

23 **ORCID**
24
25

26
27 R.C: 0000-0001-6169-530X
28
29

30
31 P.B: 0000-0002-1488-2257
32
33

34
35 I.M: 0000-0001-8342-6629
36
37
38

39
40 J.D: 0000-0002-9520-1555
41
42
43

44
45 L.D: 0000-0001-9520-1435
46
47

48
49 F.M: 0000-0002-2325-6645
50
51

52 **Author contributions**
53
54

55
56 All authors discussed the results and contributed to the final manuscript.
57
58
59
60

1
2
3
4 CONFLICT OF INTEREST
5
6

7 The authors declare no competing financial interest
8
9

10
11 ASSOCIATED CONTENT
12
13

14
15 **Supporting Information.**
16
17

18
19 The Supporting Information is available free of charge via the Internet at
20
21

22
23 <http://pubs.acs.org>. It includes:
24
25

26
27 -Discussion on the extraction of the microstrain parameter from powder X-ray
28
29

30
31 diffraction experiments with the Rietveld method
32
33

34
35 -Discussion on the correction of the as-measured microstrain to describe surface
36
37

38
39 defectiveness.
40
41

42
43 -A plot bridging the specific activity for the ORR and the $Q_{CO}/2Q_H$ ratio
44
45
46

47
48 ACKNOWLEDGEMENTS
49
50

51
52 This work was performed within the framework of the Centre of Excellence of
53
54

55
56 Multifunctional Architected Materials 'CEMAM' (grant number ANR-10-LABX-44-
57
58
59
60

1
2
3
4 01). The authors acknowledge financial support from the French National Research
5
6
7 Agency through the BRIDGE project (grant number ANR-19-ENER-0008-01).
8
9
10
11
12
13

14
15 REFERENCES
16
17
18

- 19 (1) Li, W.; Wang, D.; Zhang, Y.; Tao, L.; Wang, T.; Zou, Y.; Wang, Y.; Chen, R.;
20
21
22 Wang, S. Defect Engineering for Fuel-Cell Electrocatalysts. *Adv. Mater.* **2020**,
23
24
25
26 1907879.
27
28
29
30 (2) Nørskov, J. K.; Bligaard, T.; Rossmeisl, J.; Christensen, C. H. Towards the
31
32
33
34 Computational Design of Solid Catalysts. *Nat. Chem.* **2009**, *1* (1), 37–46.
35
36
37
38 (3) Zhao, Z.; Liu, S.; Zha, S.; Cheng, D.; Studt, F.; Henkelman, G.; Gong, J. Theory-
39
40
41
42 Guided Design of Catalytic Materials Using Scaling Relationships and Reactivity
43
44
45
46 Descriptors. *Nat. Rev. Mater.* **2019**, *4*, 792–804.
47
48
49 (4) Nørskov, J. K.; Rossmeisl, J.; Logadottir, a.; Lindqvist, L.; Kitchin, J. R.;
50
51
52
53 Bligaard, T.; Jónsson, H. Origin of the Overpotential for Oxygen Reduction at a
54
55
56
57 Fuel-Cell Cathode. *J. Phys. Chem. B* **2004**, *108* (46), 17886–17892.
58
59
60

- 1
2
3
4 (5) Robinson, P. J.; Holbrook, K. A. Why Gold Is the Noblest of All the Metals.
5
6
7 *Nature* **1995**, *376* (July), 238–240.
8
9
10
11 (6) Hammer, B.; Nørskov, J. K. Electronic Factors Determining the Reactivity of
12
13
14
15 Metal Surfaces. *Surf. Sci.* **1995**, *343* (3), 211–220.
16
17
18
19 (7) Batchelor, T. A. A.; Pedersen, J. K.; Winther, S. H.; Castelli, I. E.; Jacobsen, K.
20
21
22
23 W.; Rossmeisl, J. High-Entropy Alloys as a Discovery Platform for
24
25
26
27 Electro catalysis. *Joule* **2019**, *3* (3), 834–845.
28
29
30 (8) Le Bacq, O.; Pasturel, A.; Chattot, R.; Previdello, B.; Nelayah, J.; Asset, T.;
31
32
33
34 Dubau, L.; Maillard, F. Effect of Atomic Vacancies on the Structure and the
35
36
37
38 Electro catalytic Activity of Pt-Rich/C Nanoparticles: A Combined Experimental
39
40
41
42 and Density Functional Theory Study. *ChemCatChem* **2017**, *9* (12), 2324–2338.
43
44
45 (9) Calle-Vallejo, F.; Tymoczko, J.; Colic, V.; Quang, H. V.; Pohl, M. D.;
46
47
48
49 Morgenstern, K.; Loffreda, D.; Sautet, P.; Schuhmann, W.; Bandarenka, A. S.
50
51
52
53 Finding Optimal Surface Sites on Heterogeneous Catalysts by Counting Nearest
54
55
56
57
58
59
60 (10) Ma, X.; Xin, H. Orbitalwise Coordination Number for Predicting Adsorption

- 1
2
3
4 Properties of Metal Nanocatalysts. *Phys. Rev. Lett.* **2017**, *118* (January),
5
6
7 036101.
8
9
10
11 (11) Wu, D.; Dong, C.; Zhan, H.; Du, X. Bond-Energy-Integrated Descriptor for
12
13
14 Oxygen Electrocatalysis of Transition Metal Oxides. *J. Phys. Chem. Lett.* **2018**,
15
16
17 *9*, 3387–3391.
18
19
20
21
22 (12) Rietveld, H. M. A Profile Refinement Method for Nuclear and Magnetic
23
24
25 Structures. *J. Appl. Crystallogr.* **1969**, *2*(2), 65–71.
26
27
28
29
30 (13) Chattot, R.; Bacq, O. Le; Beermann, V.; Kühl, S.; Herranz, J.; Henning, S.; Kühn,
31
32
33 L.; Asset, T.; Guétaz, L.; Renou, G.; Drnec, J.; Bordet, P.; Pasturel, A.;
34
35
36 Eychmüller, A.; Schmidt, T. J.; Strasser, P.; Dubau, L.; Maillard, F. Surface
37
38
39 Distortion as a Unifying Concept and Descriptor in Oxygen Reduction Reaction
40
41
42
43
44 Electrocatalysis. *Nat. Mater.* **2018**, *17*(9), 827–833.
45
46
47
48 (14) Billinge, S. J. L. The Rise of the X-Ray Atomic Pair Distribution Function Method:
49
50
51
52 A Series of Fortunate Events. *Philos. Trans. R. Soc. A* **2019**, *377* (2147),
53
54
55 20180413.
56
57
58
59 (15) Thompson, P.; Cox, D. E.; Hastings, J. B. Rietveld Refinement of Debye–
60

- 1
2
3 Scherrer Synchrotron X-Ray Data from Al₂O₃. *J. Appl. Crystallogr.* **1987**, *20* (2),
4
5
6
7 79–83.
8
9
10
11 (16) Harada, M.; Ikegami, R.; Kumara, L. S. R.; Kohara, S.; Sakata, O. Reverse
12
13 Monte Carlo Modeling for Local Structures of Noble Metal Nanoparticles Using
14
15 Monte Carlo Modeling for Local Structures of Noble Metal Nanoparticles Using
16
17 High-Energy XRD and EXAFS. *RSC Adv.* **2019**, *9* (51), 29511–29521.
18
19
20
21
22 (17) Chattot, R.; Asset, T.; Bordet, P.; Drnec, J.; Dubau, L.; Maillard, F. Beyond Strain
23
24 and Ligand Effects: Microstrain-Induced Enhancement of the Oxygen Reduction
25
26 and Ligand Effects: Microstrain-Induced Enhancement of the Oxygen Reduction
27
28 Reaction Kinetics on Various PtNi/C Nanostructures. *ACS Catal.* **2017**, *7*, 398–
29
30
31
32
33 408.
34
35
36
37 (18) Sneed, B. T.; Young, A. P.; Tsung, C. K. Building up Strain in Colloidal Metal
38
39
40
41 Nanoparticle Catalysts. *Nanoscale* **2015**, *7* (29), 12248–12265.
42
43
44
45 (19) Gan, L.; Yu, R.; Luo, J.; Cheng, Z.; Zhu, J. Lattice Strain Distributions in
46
47
48 Individual Dealloyed Pt-Fe Catalyst Nanoparticles. *J. Phys. Chem. Lett.* **2012**, *3*
49
50
51
52 (7), 934–938.
53
54
55
56 (20) Suzana, A. F.; Rochet, A.; Passos, A. R.; Castro Zerba, J. P.; Polo, C. C.;
57
58
59
60 Santilli, C. V.; Pulcinelli, S. H.; Berenguer, F.; Harder, R.; Maxey, E.; Meneau,

- 1
2
3
4 F. *In Situ* Three-Dimensional Imaging of Strain in Gold Nanocrystals during
5
6
7 Catalytic Oxidation. *Nanoscale Adv.* **2019**, *1* (8), 3009–3014.
8
9
10
11 (21) Nilsson Pingel, T.; Jørgensen, M.; Yankovich, A. B.; Grönbeck, H.; Olsson, E.
12
13
14 Influence of Atomic Site-Specific Strain on Catalytic Activity of Supported
15
16
17
18 Nanoparticles. *Nat. Commun.* **2018**, *9*, 2722.
19
20
21
22 (22) Yang, Y.; Chen, C. C.; Scott, M. C.; Ophus, C.; Xu, R.; Pryor, A.; Wu, L.; Sun,
23
24
25
26 F.; Theis, W.; Zhou, J.; Eisenbach, M.; Kent, P. R. C.; Sabirianov, R. F.; Zeng,
27
28
29 H.; Ercius, P.; Miao, J. Deciphering Chemical Order/Disorder and Material
30
31
32
33 Properties at the Single-Atom Level. *Nature* **2017**, *542* (7639), 75–79.
34
35
36
37 (23) Ruiz-Zepeda, F.; Gatalo, M.; Pavlišič, A.; Dražić, G.; Jovanović, P.; Bele, M.;
38
39
40
41 Gaberšček, M.; Hodnik, N. Atomically Resolved Anisotropic Electrochemical
42
43
44
45 Shaping of Nano-Electrocatalyst. *Nano Lett.* **2019**, *19* (8), 4919–4927.
46
47
48
49 (24) Stukowski, A.; Markmann, J.; Weissmüller, J.; Albe, K. Atomistic Origin of
50
51
52
53 Microstrain Broadening in Diffraction Data of Nanocrystalline Solids. *Acta Mater.*
54
55
56
57 **2009**, *57* (5), 1648–1654.
58
59
60 (25) Montejano-Carrizales, J. M.; Morán-López, J. L. Geometrical Characteristics of

- 1
2
3 Compact Nanoclusters. *Nanostructured Mater.* **1992**, *1* (5), 397–409.
4
5
6
7
8 (26) Chattot, R.; Martens, I.; Scohy, M.; Drnec, J.; Maillard, F.; Dubau, L. Disclosing
9
10 Pt-Bimetallic Alloy Nanoparticle Surface Lattice Distortion with Electrochemical
11
12 Probes. *ACS Energy Lett.* **2020**, *5* (1), 162–169.
13
14
15
16
17
18 (27) Henning, S.; Kühn, L.; Herranz, J.; Durst, J.; Binninger, T.; Nachtegaal, M.;
19
20 Werheid, M.; Liu, W.; Adam, M.; Kaskel, S.; Eychmüller, A.; Schmidt, T. J. Pt-Ni
21
22 Aerogels as Unsupported Electrocatalysts for the Oxygen Reduction Reaction.
23
24
25
26
27
28
29
30
31
32
33
34 (28) Henning, S.; Herranz, J.; Ishikawa, H.; Kim, B. J.; Abbott, D.; Kühn, L.;
35
36 Eychmüller, A.; Schmidt, T. J. Durability of Unsupported Pt-Ni Aerogels in PEFC
37
38 Cathodes. *J. Electrochem. Soc.* **2017**, *164* (12), F1136–F1141.
39
40
41
42
43
44
45 (29) Henning, S.; Ishikawa, H.; Kühn, L.; Herranz, J.; Müller, E.; Eychmüller, A.;
46
47 Schmidt, T. J. Unsupported Pt-Ni Aerogels with Enhanced High Current
48
49 Performance and Durability in Fuel Cell Cathodes. *Angew. Chemie - Int. Ed.*
50
51
52
53
54
55
56
57
58
59
60 (30) Li, M.; Zhao, Z.; Cheng, T.; Fortunelli, A.; Chen, C. Y.; Yu, R.; Zhang, Q.; Gu,

- 1
2
3 L.; Merinov, B. V.; Lin, Z.; Zhu, E.; Yu, T.; Jia, Q.; Guo, J.; Zhang, L.; Goddard,
4
5
6
7 W. A.; Huang, Y.; Duan, X. Ultrafine Jagged Platinum Nanowires Enable
8
9
10 Ultrahigh Mass Activity for the Oxygen Reduction Reaction. *Science* **2016**, *354*
11
12
13
14 (6318), 1414–1419.
15
16
17
18 (31) Alia, S. M.; Ngo, C.; Shulda, S.; Ha, M. A.; Dameron, A. A.; Weker, J. N.;
19
20
21 Neyerlin, K. C.; Kocha, S. S.; Pylypenko, S.; Pivovar, B. S. Exceptional Oxygen
22
23
24
25 Reduction Reaction Activity and Durability of Platinum-Nickel Nanowires
26
27
28 through Synthesis and Post-Treatment Optimization. *ACS Omega* **2017**, *2* (4),
29
30
31
32 1408–1418.
33
34
35
36 (32) Van Der Vliet, D. F.; Wang, C.; Tripkovic, D.; Strmcnik, D.; Zhang, X. F.; Debe,
37
38
39
40 M. K.; Atanasoski, R. T.; Markovic, N. M.; Stamenkovic, V. R. Mesostructured
41
42
43
44 Thin Films as Electrocatalysts with Tunable Composition and Surface
45
46
47
48 Morphology. *Nat. Mater.* **2012**, *11* (12), 1051–1058.
49
50
51 (33) Bae, S. J.; Yoo, S. J.; Lim, Y.; Kim, S.; Lim, Y.; Choi, J.; Nahm, K. S.; Hwang,
52
53
54
55 S. J.; Lim, T. H.; Kim, S. K.; Kim, P. Facile Preparation of Carbon-Supported
56
57
58
59 PtNi Hollow Nanoparticles with High Electrochemical Performance. *J. Mater.*
60

- 1
2
3
4 *Chem.* **2012**, *22* (18), 8820–8825.
5
6
7
8 (34) Snyder, J.; Fujita, T.; Chen, M. W.; Erlebacher, J. Oxygen Reduction in
9
10 Nanoporous Metal-Ionic Liquid Composite Electrocatalysts. *Nat. Mater.* **2010**, *9*
11
12 (11), 904–907.
13
14
15
16
17
18
19 (35) Luo, M.; Sun, Y.; Zhang, X.; Qin, Y.; Li, M.; Li, Y.; Li, C.; Yang, Y.; Wang, L.;
20
21 Gao, P.; Lu, G.; Guo, S. Stable High-Index Faceted Pt Skin on Zigzag-Like PtFe
22
23 Nanowires Enhances Oxygen Reduction Catalysis. *Adv. Mater.* **2018**, *30* (10),
24
25 1705515.
26
27
28
29
30
31
32
33
34 (36) Dubau, L.; Nelayah, J.; Moldovan, S.; Ersen, O.; Bordet, P.; Drnec, J.; Asset, T.;
35
36 Chattot, R.; Maillard, F. Defects Do Catalysis: CO Monolayer Oxidation and
37
38 Oxygen Reduction Reaction on Hollow PtNi/C Nanoparticles. *ACS Catal.* **2016**,
39
40 *6* (7), 4673–4684.
41
42
43
44
45
46
47
48 (37) Alia, S. M.; Pylypenko, S.; Neyerlin, K. C.; Kocha, S. S.; Pivovar, B. S. Nickel
49
50 Nanowire Oxidation and Its Effect on Platinum Galvanic Displacement and
51
52 Methanol Oxidation. *ECS Trans.* **2014**, *64* (3), 89–95.
53
54
55
56
57
58
59
60 (38) Xiong, Z.; Li, S.; Xu, H.; Zhang, K.; Yan, B.; Du, Y. Newly Designed Ternary

- 1
2
3
4 Metallic PtPdBi Hollow Catalyst with High Performance for Methanol and
5
6
7 Ethanol Oxidation. *Catalysts* **2017**, *7*, 208.
8
9
10
11 (39) Mao, J.; Chen, W.; He, D.; Wan, J.; Pei, J.; Dong, J.; Wang, Y.; An, P.; Jin, Z.;
12
13
14 Xing, W.; Tang, H.; Zhuang, Z.; Liang, X.; Huang, Y.; Zhou, G.; Wang, L.; Wang,
15
16
17 D.; Li, Y. Design of Ultrathin Pt-Mo-Ni Nanowire Catalysts for Ethanol
18
19
20
21 Electrooxidation. *Sci. Adv.* **2017**, *3*, e1603068.
22
23
24
25
26 (40) Zhao, S.; Li, M.; Han, M.; Xu, D.; Yang, J.; Lin, Y.; Shi, N. E.; Lu, Y.; Yang, R.;
27
28
29 Liu, B.; Dai, Z.; Bao, J. Defect-Rich Ni₃FeN Nanocrystals Anchored on N-Doped
30
31
32
33 Graphene for Enhanced Electrocatalytic Oxygen Evolution. *Adv. Funct. Mater.*
34
35
36
37 **2017**, *28* (18), 1706018.
38
39
40
41 (41) Wang, P.; Jiang, K.; Wang, G.; Yao, J.; Huang, X. Phase and Interface
42
43
44 Engineering of Platinum–Nickel Nanowires for Efficient Electrochemical
45
46
47 Hydrogen Evolution. *Angew. Chemie - Int. Ed.* **2016**, *55* (41), 12859–12863.
48
49
50
51
52 (42) Dickens, C. F.; Nørskov, J. K. A Theoretical Investigation into the Role of
53
54
55
56 Surface Defects for Oxygen Evolution on RuO₂. *J. Phys. Chem. C* **2017**, *121*
57
58
59 (34), 18516–18524.
60

- 1
2
3
4 (43) Shi, Q.; Zhu, C.; Zhong, H.; Su, D.; Li, N.; Engelhard, M. H.; Xia, H.; Zhang, Q.;
5
6
7 Feng, S.; Beckman, S. P.; Du, D.; Lin, Y. Nanovoid Incorporated Ir_xCu Metallic
8
9
10 Aerogels for Oxygen Evolution Reaction Catalysis. *ACS Energy Lett.* **2018**, *3*
11
12
13
14 (9), 2038–2044.
15
16
17
18 (44) Calle-Vallejo, F.; Pohl, M. D.; Bandarenka, A. S. Quantitative Coordination-
19
20
21 Activity Relations for the Design of Enhanced Pt Catalysts for CO Electro-
22
23
24 Oxidation. *ACS Catal.* **2017**, *7*(7), 4355–4359.
25
26
27
28
29 (45) Maillard, F.; Eikerling, M.; Cherstiouk, O. V.; Schreier, S.; Savinova, E.;
30
31
32 Stimming, U. Size Effects on Reactivity of Pt Nanoparticles in CO Monolayer
33
34
35 Oxidation: The Role of Surface Mobility. *Faraday Discuss.* **2004**, *125*, 357–377.
36
37
38
39
40 (46) Van Der Vliet, D. F.; Wang, C.; Li, D.; Paulikas, A. P.; Greeley, J.; Rankin, R. B.;
41
42
43 Strmcnik, D.; Tripkovic, D.; Markovic, N. M.; Stamenkovic, V. R. Unique
44
45
46 Electrochemical Adsorption Properties of Pt-Skin Surfaces. *Angew. Chemie -*
47
48
49 *Int. Ed.* **2012**, *51*(13), 3139–3142.
50
51
52
53
54
55 (47) Marichev, V. A. Reversibility of Platinum Voltammograms in Aqueous
56
57
58 Electrolytes and Ionic Product of Water. *Electrochim. Acta* **2008**, *53*(27), 7952–
59
60

- 1
2
3
4 7960.
5
6
7
8 (48) Van Der Niet, M. J. T. C.; Garcia-Araez, N.; Hernández, J.; Feliu, J. M.; Koper,
9
10
11 M. T. M. Water Dissociation on Well-Defined Platinum Surfaces: The
12
13
14 Electrochemical Perspective. *Catal. Today* **2013**, *202*, 105–113.
15
16
17
18
19 (49) Janik, M. J.; McCrum, I. T.; Koper, M. T. M. On the Presence of Surface Bound
20
21
22 Hydroxyl Species on Polycrystalline Pt Electrodes in the “Hydrogen Potential
23
24
25
26 Region” (0 to 0.4 V-RHE). *J. Catal.* **2018**, *367*, 332–337.
27
28
29
30 (50) Tanaka, H.; Sugawara, S.; Shinohara, K.; Ueno, T.; Suzuki, S.; Hoshi, N.;
31
32
33 Nakamura, M. Infrared Reflection Absorption Spectroscopy of OH Adsorption
34
35
36 on the Low Index Planes of Pt. *Electrocatalysis* **2015**, *6* (3), 295–299.
37
38
39
40
41 (51) Garcia-Araez, N.; Climent, V.; Feliu, J. M. Analysis of Temperature Effects on
42
43
44 Hydrogen and OH Adsorption on Pt(111), Pt(100) and Pt(110) by Means of
45
46
47 Gibbs Thermodynamics. *J. Electroanal. Chem.* **2010**, *649* (1–2), 69–82.
48
49
50
51
52 (52) Zhang, C.; Firestein, K. L.; Fernando, J. F. S.; Siriwardena, D.; von Treifeldt, J.
53
54
55
56 E.; Golberg, D. Recent Progress of *In Situ* Transmission Electron Microscopy
57
58
59 for Energy Materials. *Adv. Mater.* **2019**, *32* (18), 1904094.
60

- 1
2
3
4 (53) Daio, T.; Staykov, A.; Guo, L.; Liu, J.; Tanaka, M.; Matthew Lyth, S.; Sasaki, K.
5
6
7 Lattice Strain Mapping of Platinum Nanoparticles on Carbon and SnO₂
8
9
10 Supports. *Sci. Rep.* **2015**, *5*, 13126.
11
12
13
14 (54) Wang, Y.; Zhang, W. Mapping the Strain Distribution within Embedded
15
16
17 Nanoparticles via Geometrical Phase Analysis. *Micron* **2019**, *125*, 102715.
18
19
20
21
22 (55) Ahmad, N.; Le Bouar, Y.; Ricolleau, C.; Alloyeau, D. Growth of Dendritic
23
24
25
26 Nanostructures by Liquid-Cell Transmission Electron Microscopy: A Reflection
27
28
29 of the Electron-Irradiation History. *Adv. Struct. Chem. Imaging* **2016**, *2*, 9.
30
31
32
33 (56) Kelly, T. F.; Miller, M. K. Atom Probe Tomography. *Rev. Sci. Instrum.* **2007**, *78*,
34
35
36
37 031101.
38
39
40
41 (57) Gault, B.; Breen, A. J.; Chang, Y.; He, J.; Jäggle, E. A.; Kontis, P.; Kürnsteiner,
42
43
44
45 P.; Kwiatkowski Da Silva, A.; Makineni, S. K.; Mouton, I.; Peng, Z.; Ponge, D.;
46
47
48
49 Schwarz, T.; Stephenson, L. T.; Szczepaniak, A.; Zhao, H.; Raabe, D. Interfaces
50
51
52 and Defect Composition at the Near-Atomic Scale through Atom Probe
53
54
55 Tomography Investigations. *J. Mater. Res.* **2018**, *33* (23), 4018–4030.
56
57
58
59 (58) Li, T.; Bagot, P. A. J.; Marquis, E. A.; Tsang, S. C. E.; Smith, G. D. W.
60

- 1
2
3
4 Characterization of Oxidation and Reduction of Pt-Ru and Pt-Rh-Ru Alloys by
5
6
7 Atom Probe Tomography and Comparison with Pt-Rh. *J. Phys. Chem. C* **2012**,
8
9
10 *116* (33), 17633–17640.
11
12
13
14
15 (59) Li, T.; Kasian, O.; Cherevko, S.; Zhang, S.; Geiger, S.; Scheu, C.; Felfer, P.;
16
17
18 Raabe, D.; Gault, B.; Mayrhofer, K. J. J. Atomic-Scale Insights into Surface
19
20
21
22 Species of Electrocatalysts in Three Dimensions. *Nat. Catal.* **2018**, *1* (4), 300–
23
24
25 305.
26
27
28
29 (60) Wilde, P.; Dieckhöfer, S.; Quast, T.; Xiang, W.; Bhatt, A.; Chen, Y. T.; Seisel, S.;
30
31
32
33 Barwe, S.; Andronescu, C.; Li, T.; Schuhmann, W.; Masa, J. Insights into the
34
35
36
37 Formation, Chemical Stability, and Activity of Transient Ni_yP@NiO_x Core-Shell
38
39
40
41 Heterostructures for the Oxygen Evolution Reaction. *ACS Appl. Energy Mater.*
42
43
44 **2020**, *3* (3), 2304–2309.
45
46
47
48 (61) Barroo, C.; Akey, A. J.; Bell, D. C. Atom Probe Tomography for Catalysis
49
50
51
52 Applications: A Review. *Appl. Sci.* **2019**, *9* (13), 2721.
53
54
55
56 (62) Pfeiffer, B.; Erichsen, T.; Epler, E.; Volkert, C. A.; Trompenaars, P.; Nowak, C.
57
58
59
60 Characterization of Nanoporous Materials with Atom Probe Tomography.

- 1
2
3
4 *Microsc. Microanal.* **2015**, *21* (3), 557–563.
5
6
7
- 8 (63) Tedsree, K.; Li, T.; Jones, S.; Chan, C. W. A.; Yu, K. M. K.; Bagot, P. A. J.;
9
10
11 Marquis, E. A.; Smith, G. D. W.; Tsang, S. C. E. Hydrogen Production from
12
13 Formic Acid Decomposition at Room Temperature Using a Ag-Pd Core-Shell
14
15
16
17
18 Nanocatalyst. *Nat. Nanotechnol.* **2011**, *6* (5), 302–307.
19
20
21
- 22 (64) Abbey, B. From Grain Boundaries to Single Defects: A Review of Coherent
23
24
25
26
27
28
29
30
31
32
33
34
35
36
37
38
39
40
41
42
43
44
45
46
47
48
49
50
51
52
53
54
55
56
57
58
59
60
- (65) Ulvestad, A.; Tripathi, A.; Hruszkewycz, S. O.; Cha, W.; Wild, S. M.;
Stephenson, G. B.; Fuoss, P. H. Coherent Diffractive Imaging of Time-Evolving
Samples with Improved Temporal Resolution. *Phys. Rev. B* **2016**, *93* (18),
184105.
- (66) Carnis, J.; Gao, L.; Labat, S.; Kim, Y. Y.; Hofmann, J. P.; Leake, S. J.; Schüllli,
T. U.; Hensen, E. J. M.; Thomas, O.; Richard, M.-I. Towards a Quantitative
Determination of Strain in Bragg Coherent X-Ray Diffraction Imaging: Artefacts
and Sign Convention in Reconstructions. *Sci. Rep.* **2019**, *9*, 17357.

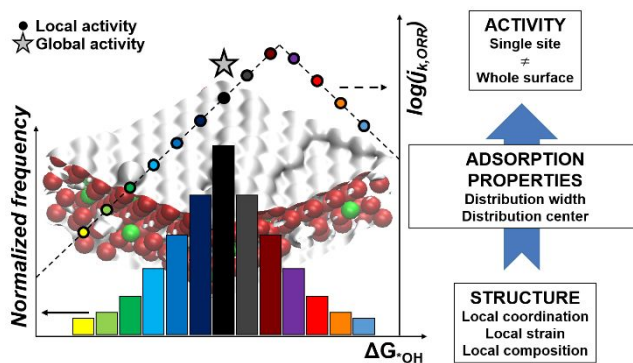
- 1
2
3
4 (67) Ulvestad, U.; Singer, A.; Clark, J. N.; Cho, H. M.; Kim, J. W.; Harder, R.; Maser,
5
6
7 J.; Meng, Y. S.; Shpyrko, O. G. Topological Defect Dynamics in *Operando*
8
9
10 Battery Nanoparticles. *Science* **2015**, *348* (6241), 1344–1347.
11
12
13
14 (68) Abuin, M.; Kim, Y. Y.; Runge, H.; Kulkarni, S.; Maier, S.; Dzhigaev, D.; Lazarev,
15
16
17 S.; Gelisio, L.; Seitz, C.; Richard, M.-I.; Zhou, T.; Vonk, V.; Keller, T. F.;
18
19
20 Vartanyants, I. A.; Stierle, A. Coherent X-Ray Imaging of CO-Adsorption-
21
22
23 Induced Structural Changes in Pt Nanoparticles: Implications for Catalysis. *ACS*
24
25
26
27
28
29 *Appl. Nano Mater.* **2019**, *2* (8), 4818–4824.
30
31
32
33 (69) Kim, D.; Chung, M.; Kim, S.; Yun, K.; Cha, W.; Harder, R.; Kim, H. Defect
34
35
36 Dynamics at a Single Pt Nanoparticle during Catalytic Oxidation. *Nano Lett.*
37
38
39
40 **2019**, *19* (8), 5044–5052.
41
42
43
44 (70) Sun, Y.; Liang, Y.; Luo, M.; Lv, F.; Qin, Y.; Wang, L.; Xu, C.; Fu, E.; Guo, S.
45
46
47 Defects and Interfaces on PtPb Nanoplates Boost Fuel Cell Electrocatalysis.
48
49
50
51 *Small* **2018**, *14* (3), 1702259.
52
53
54
55 (71) Fichtner, J.; Watzele, S.; Garlyyev, B.; Kluge, R. M.; Haimerl, F.; El-Sayed, H.
56
57
58
59 A.; Li, W. J.; Maillard, F. M.; Dubau, L.; Chattot, R.; Michalička, J.; MacAk, J. M.;
60

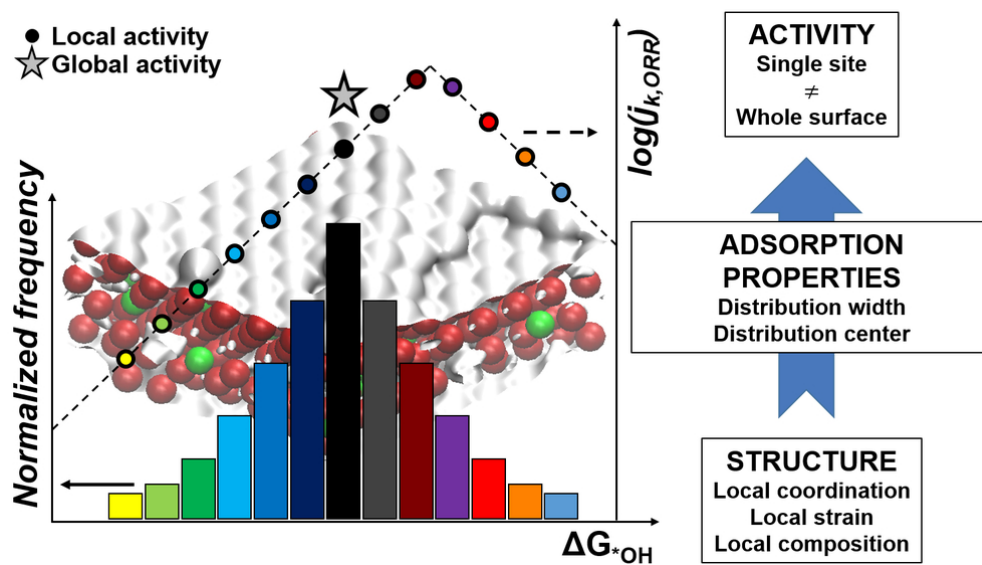
- 1
2
3
4 Wang, W.; Wang, D.; Gigl, T.; Hugenschmidt, C.; Bandarenka, A. S. Tailoring
5
6
7 the Oxygen Reduction Activity of Pt Nanoparticles through Surface Defects: A
8
9
10 Simple Top-Down Approach. *ACS Catal.* **2020**, *10* (5), 3131–3142.
11
12
13
14
15 (72) Dou, S.; Tao, L.; Wang, R.; El Hankari, S.; Chen, R.; Wang, S. Plasma-Assisted
16
17
18 Synthesis and Surface Modification of Electrode Materials for Renewable
19
20
21 Energy. *Adv. Mater.* **2018**, *30* (21), 1705850.
22
23
24
25
26 (73) Ruge, M.; Drnec, J.; Rahn, B.; Reikowski, F.; Harrington, D. A.; Carlà, F.; Felici,
27
28
29 R.; Stettner, J.; Magnussen, O. M. Structural Reorganization of Pt(111)
30
31
32 Electrodes by Electrochemical Oxidation and Reduction. *J. Am. Chem. Soc.*
33
34
35
36 **2017**, *139* (12), 4532–4539.
37
38
39
40
41 (74) Jacobse, L.; Huang, Y. F.; Koper, M. T. M.; Rost, M. J. Correlation of Surface
42
43
44 Site Formation to Nanoisland Growth in the Electrochemical Roughening of
45
46
47 Pt(111). *Nat. Mater.* **2018**, *17* (3), 277–282.
48
49
50
51
52 (75) Jacobse, L.; Rost, M. J.; Koper, M. T. M. Atomic-Scale Identification of the
53
54
55 Electrochemical Roughening of Platinum. *ACS Cent. Sci.* **2019**, *5* (12), 1920–
56
57
58
59 1928.
60

- 1
2
3
4 (76) Livet, F.; Beutier, G.; De Boissieu, M.; Ravy, S.; Picca, F.; Le Bolloc'H, D.;
5
6
7 Jacques, V. Coherent Scattering from Silicon Monocrystal Surface. *Surf. Sci.*
8
9
10 **2011**, *605*, 390–395.
11
12
13
14
15 (77) Nicolas, J. D.; Reusch, T.; Osterhoff, M.; Sprung, M.; Schülein, F. J. R.; Krenner,
16
17
18 H. J.; Wixforth, A.; Salditt, T. Time-Resolved Coherent X-Ray Diffraction Imaging
19
20
21 of Surface Acoustic Waves. *J. Appl. Crystallogr.* **2014**, *47*(5), 1596–1605.
22
23
24
25
26 (78) Kutsal, M.; Bernard, P.; Berruyer, G.; Cook, P. K.; Hino, R. The ESRF Dark-
27
28
29 Field x-Ray Microscope at ID06. *IOP Conf. Ser. Mater. Sci. Eng.* **2019**, *580*,
30
31
32 012007.
33
34
35
36
37 (79) Morgan, A. J.; Prasciolu, M.; Andrejczuk, A.; Krzywinski, J.; Meents, A.;
38
39
40 Pennicard, D.; Graafsma, H.; Barty, A.; Bean, R. J.; Barthelmess, M.; Oberthuer,
41
42
43 D.; Yefanov, O.; Aquila, A.; Chapman, H. N.; Bajt, S. High Numerical Aperture
44
45
46
47 Multilayer Laue Lenses. *Sci. Rep.* **2015**, *5*, 9892.
48
49
50
51
52 (80) Pfisterer, J. H. K.; Liang, Y.; Schneider, O.; Bandarenka, A. S. Direct
53
54
55 Instrumental Identification of Catalytically Active Surface Sites. *Nature* **2017**,
56
57
58 *549*(7670), 74–77.
59
60

- 1
2
3
4 (81) Sumetskii, M.; Kornyshev, A. A.; Stimming, U. Adatom Diffusion Characteristics
5
6
7 from STM Noise: Theory. *Surf. Sci.* **1994**, *307–309*, 23–27.
8
9
10
11 (82) Sumetskii, M.; Kornyshev, A. A. Noise in STM Due to Atoms Moving in the
12
13
14 Tunneling Space. *Phys. Rev. B* **1993**, *48* (23), 17493–17506.
15
16
17
18
19 (83) Hugelmann, M.; Schindler, W. Tunnel Barrier Height Oscillations at the
20
21
22 Solid/Liquid Interface. *Surf. Sci.* **2003**, *541*, L643–L648.
23
24
25
26
27 (84) Liang, Y.; McLaughlin, D.; Csoklich, C.; Schneider, O.; Bandarenka, A. S. The
28
29
30 Nature of Active Centers Catalyzing Oxygen Electro-Reduction at Platinum
31
32
33 Surfaces in Alkaline Media. *Energy Environ. Sci.* **2019**, *12* (1), 351–357.
34
35
36
37
38 (85) Mitterreiter, E.; Liang, Y.; Golibrzuch, M.; McLaughlin, D.; Csoklich, C.; Bartl, J.
39
40
41 D.; Holleitner, A.; Wurstbauer, U.; Bandarenka, A. S. *In-Situ* Visualization of
42
43
44 Hydrogen Evolution Sites on Helium Ion Treated Molybdenum Dichalcogenides
45
46
47
48 under Reaction Conditions. *npj 2D Mater. Appl.* **2019**, *3* (25).
49
50
51
52
53
54
55
56
57
58
59
60

FOR TABLE OF CONTENTS ONLY





Every Piece Matters: Describing and quantifying surface structural disorder is essential for rationalizing the catalytic performance of defect-engineered nanocatalysts.

84x47mm (300 x 300 DPI)